First-principles surface characterization and water adsorption of Fe_3P schreibersite

Riccardo Dettori*,† and Nir Goldman*,†,‡

†*Physical and Life Sciences Directorate, Lawrence Livermore National Laboratory, 7000 East Avenue, Livermore, California 94550, United States*

‡*Department of Chemical Engineering, University of California, Davis, California 95616, United States*

E-mail: dettori1@llnl.gov; ngoldman@llnl.gov

Abstract

The meteoritic mineral schreibersite, e.g., Fe_3P, is a proposed abiotic source of phosphorus for phosphate ion (PO_4^-) production, needed for nucleobases, phospholipids, and other life building materials. Schreibersite could have acted as both a source of elemental phosphorus and as a catalyst, and the hostile conditions on early Earth could have accelerated its degradation in different environments. Here, we present results from quantum calculations of bulk schreibersite and of its low Miller index surfaces. We also investigate water surface adsorption and identify possible dissociation pathways on the most stable facet. Our calculations provide useful chemical insights into schreibersite interactions in aqueous environments, paving the way for further detailed investigation on more reactive surfaces. Our results help provide a "bottom-up" understanding for phosphorylated organic synthesis on the primitive planet and its role in producing life building molecules.

Introduction

Debate over the origins of prebiotic organic material (e.g., amino acids, lipids, nucleotides, etc.) on early Earth has been a subject of intense study for numerous decades. Considerable effort has focused on synthesis from materials already in existence on the primitive planet. Initial experimentation observed amino acid synthesis in vaporized hydrogen-rich mixtures subjected to electrical discharges.[1–3] Prebiotic organic material has additionally been synthesized under high-temperature conditions in the presence of hydrogen gas (e.g., Refs.[4,5]). Aqueous mixtures subjected to UV radiation[6–8] and shock compression[9,10] have produced amino acids and precursors to DNA and RNA nucleobases. Shock compression and mechanochemical shearing have been shown to drive the synthesis of complex organics.[11–15] Despite these types of advances, to date the process by which the biologically vital element phosphorus was incorporated into life-building organic materials is still largely unknown.

Phosphorus is one of the key elements in modern biochemistry, in which it fills many different roles.[16–18] It forms the backbone of nucleotides (the monomer units of DNA and RNA), which contain subunits of a nitrogenous nucleobase, a five carbon sugar, and at least one phosphate (PO_4^-) group. Oxidized forms of phosphorus also comprise an important part of phospholipids, which are an essential component of cellular membrane lipid bilayers. Biological systems store metabolic energy through adenosine triphosphate (ATP), and phosphate ions combine with calcium to form apatite, the main mineral component of bone. Hence, biologically active forms of organophosphates generally contain phosphate ions or other oxidized forms of the element. In contrast, phosphate containing minerals are generally insoluble in water, which in turn could hamper their ability to have contributed to organic reactivity in a primitive environment. As a result, there exists a so-called 'phosphate problem',[16] wherein the production of phosphate and its incorporation into biological precursors on early Earth is still largely unknown.

The mineral schreibersite, $(Fe,Ni)_3$-P, has been suggested as one possible source of phosphorus for eventual phosphorylation of prebiotic organics.[16,19,20] It is common to iron-nickel

meteorites and could have contributed as much as 10% of the phosphorus likely present in the Hadean crust.[17] Schreibersite is a crystalline material with a tetragonal lattice structure (Fig. 1a). Its surfaces allows for the adsorption of water or other molecules in a number of different sites, potentially exposing elemental phosphorous to various chemical reactions. In addition, the transition metal ions within the material can act as a catalysts for organic chemical reactivity,[17] including the synthesis of phosphorylated nucleosides (nucleic acid precursors)[20] and phosphocholine (membrane precursor).[21]

In contrast to apatite, schreibersite is known to corrode in aqueous systems, producing a number of phosphorus oxanions, including phosphate.[22] Consequently, its presence in reactive environments on early Earth could have led to the synthesis of organophosphate compounds. To date, prebiotic studies with schreibersite have generally been limited to moderate temperatures and neutral or weakly basic conditions.[23,24] Little is known about the initial stages of aqueous corrosion, including the kinetic parameters, likely corrosion initiation points, and temperature dependent rates that govern its decomposition. In addition, early Earth likely experienced an enormous range of thermodynamic conditions, where wildly fluctuating thermodynamic conditions could have driven the formation of metastable compounds.[11,12,25] Thus, prebiotic schreibersite studies would greatly benefit from detailed information regarding reaction mechanisms on given nanoparticulates and/or grain boundaries, and temperature dependent rate laws that can be used for larger scale models.

Quantum calculations can help elucidate these types of discoveries by yielding electronic and/or atomic-level information about potential reaction pathways in condensed phases.[15,26] This can include simple descriptions of ionized intermediates, heats of reactions, and Arrhenius kinetic parameters. These types of results can make experiments more tractable by aiding in their interpretation, and helping to narrow the number of possible schreibersite degradation mechanisms that are likely present in dynamic environments. In particular, Kohn-Sham Density Functional Theory (DFT) calculations have demonstrated strong ability in accurately reproducing the bulk properties and thermal decomposition of many materi-

als over a broad range of chemical and thermodynamic conditions,[11,26,27] particularly for condensed phases and their surface properties.[28]

To this effect, we have performed a series of quantum calculations of the initial steps of schreibersite corrosion in aqueous systems on its most stable facet. We first discuss results regarding our choice of DFT basis set size and other parameters in terms of the predicted bulk lattice constants, electron density of states, bulk modulus, and low index surface energies. We then determine water adsorption properties in different surface sites, and compute approximate dissociation pathways for different scenarios. Ultimately, our goal is to help bound the picture of how the presence of water under highly reactive conditions could have enhanced the formation of prebiological compounds containing phosphorus.

Methods

All DFT simulations were performed with the VASP *ab initio* simulation package,[29–31] using the projector augmented wave (PAW) method[32,33] and the Perdew, Burke, and Ernzerhof exchange-correlation functional (PBE).[34] Partial occupancies of the electronic states were set with fourth-order Methfessel-Paxton smearing,[35] using a width of 0.2 eV. We observed converged energies for the bulk system with a plane-wave energy cut-off of 500 eV, with a self-consistent field (SCF) convergence criteria of 10^{-6} eV. The force convergence tolerance was set to 0.01 eV/Å for each atom in each direction. Calculations were performed with collinear spin polarization in all cases, resulting in a ferromagnetic system. During optimization, we let both atomic positions and cell parameters relax for the bulk system, while the simulation cell was kept fixed for the slab surfaces. A $6 \times 6 \times 6$ **k**-point Monkhorst-Pack mesh sampling of Brillouin zone[36] was used for the bulk calculations, while a $1 \times 7 \times 7$ mesh was used for the surface calculations, where the smaller mesh value is related to the non-periodic surface direction (see Fig. S1 in the Supporting Information for benchmarking studies on plane-wave energy cut-off and on the number of **k**-points performed on bulk schreibersite).

In order to account for electronic correlations more accurately, we adopted the rotationally invariant approach to LSDA+U of Ref. 37, with a $U - J$ value of 1.30 eV. This value was chosen to yield unit cell parameters in good agreement with experimental results (discussed below). However, since the inclusion of the LSDA+U on-site repulsion can enhance computational cost during optimization, especially when dealing with finite systems such as surface slabs, we omitted this correction for our water surface adsorption calculations. Previous DFT efforts for surface adsorption of atmospheric gases on metallic surfaces show that the LSDA+U term yields little change in the adsorption energies.[38] In order to assess the validity of this assumption, we provide comparison to results for some reference properties (i.e., bulk energy, surface formation energy) from the 'standard', non-corrected DFT approach. Surface slabs and adsorbate/surface complexes were generated by means of PyMatGen,[39–41] while atomistic renderings were obtained with VMD[42] and VESTA.[43]

Results and discussion

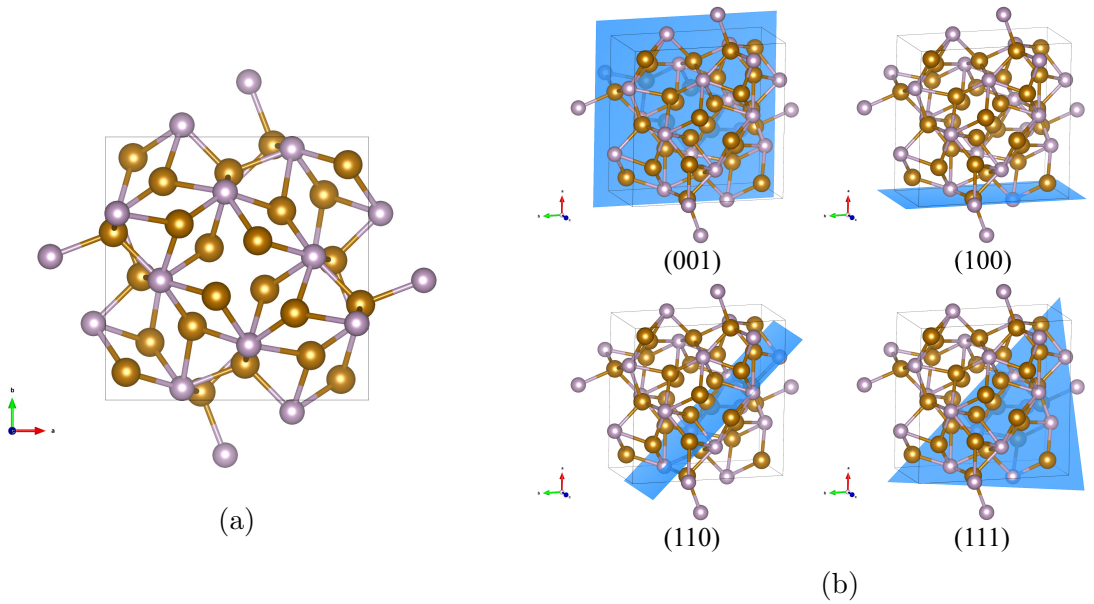

Figure 1: (a) (*ab*) view of the optimized bulk schreibersite. Fe atoms are represented in gold, P atoms in purple. (b) Renderings of the low Miller index crystal facets considered in our study.

Table 1: Cell parameters of bulk schreibersite, with comparison between experimental and calculated values, with or without Hubbard correction. Experimental uncertainties are reported in parentheses.

	a (Å)	c (Å)	volume (Å^3)
expt.[44]	9.099(2)	4.463(2)	369.5(2)
expt.[45]	9.1003(1)	4.4685(1)	370.065(6)
LSDA+U	9.081	4.380	361.2
LSDA	9.045	4.380	358.3

The bulk structure of schreibersite, which is shown in Fig. 1a, crystallizes in the non-centrosymmetric (tetragonal) space group $I\bar{4}$ ($a = b \neq c$ and $\alpha = \beta = \gamma = 90°$). We used a 32 atom supercell for our bulk lattice parameter calculations. We observe that our results from both standard and LSDA+U approaches yield lattice constants that agree within ∼1% or less of experimental results. Both approaches yield a slightly more dense structure with respect to experiment, similar to previous results for nickel-containing schreibersite ($(Fe_2, Ni)P$).[46]

We have further validated our approach by computing the zero temperature cold curve up to 20 GPa, with comparison to experimental data.[44,45] We have also computed the bulk modulus by fitting our data with a second order Birch-Murnaghan[47,48] equation of state. In both cases, our computed results with and without the LSDA+U correction are in good agreement with experimental measurements (Fig. 2a). We note that the choice of LSDA+U correction provides lattice constants slightly closer to the experimental values, but does not show significant impact on the bulk modulus since both results are within the range of experimental results.

We also observe that the bulk modulus from our LSDA+U calculations resulted in a lower value than that from standard DFT (implying a slightly less stiff structure). This is consistent with previous works, which indicate that inclusion of this on-site extra-repulsion for d-orbitals on metal atoms can result in a softer predicted bulk modulus for many materials.[49] Our results could be refined further through use of methods that include additional orbital repulsions,[50] which is beyond the scope of the current work.

Finally, in order to probe potential differences in the electronic structure from each

approach, we have computed the total electronic density of states (DOS) from both standard and LSDA+U (Fig. 2b). Our results indicate show that both methods yield a ferromagnetic material of similar magnitude (as indicated by the similarities between the differences of the area under the spin-up and spin-down curves). Small differences exist between the methods for the spin-up DOS from around -4 eV and up, though these appear minor from this comparison. Hence, we estimate similar bulk electronic properties from each method.

We now proceed with determination of appropriate slab structures for surface characterization and chemistry. In this regard, we built several low index schreibersite surface facets, namely (001), (100), (110) and (111) (Fig. 1b). Due to its bi-elemental nature, each facet can be constructed with different surface terminations (i.e., the number of P or Fe atoms at the surface). Hence, for this work we have adopted a surface construction ruleset for each crystal orientation where an eligible facet must satisfy both symmetry (top and bottom layers are identical) and stoichiometry (i.e., the facet does not require additional terminations to prevent a surface dipole moment and maintains a 3:1 iron to phosphorus ratio). This resulted in two different surface for each facet, where either a majority of iron (labeled 'type 1') or phosphorus atoms (labeled 'type 2') were present.

We then determined the most stable form of each crystalline facet by computing the surface formation energy E_{surface}, defined as:

$$E_{\text{surface}} = \frac{E_{\text{slab}} - n\left(\frac{E_{\text{bulk}}}{n_{\text{bulk}}}\right)}{2A}. \tag{1}$$

Here, E_{slab} is the total electronic energy of the slab, $(E_{\text{bulk}}/n_{\text{bulk}})$ is the energy per atom of the bulk cell, n is the number of atoms contained in the slab, and A is the surface area of a given facet. We also thoroughly tested the convergence of the surface energy with respect to the vacuum space thickness, in order to minimize nonphysical interactions between periodic images. Our tests indicate that our surface calculations are converged with schreibersite slabs of 6 atomic layers (corresponding to a total of 96 atoms) and with a vacuum region

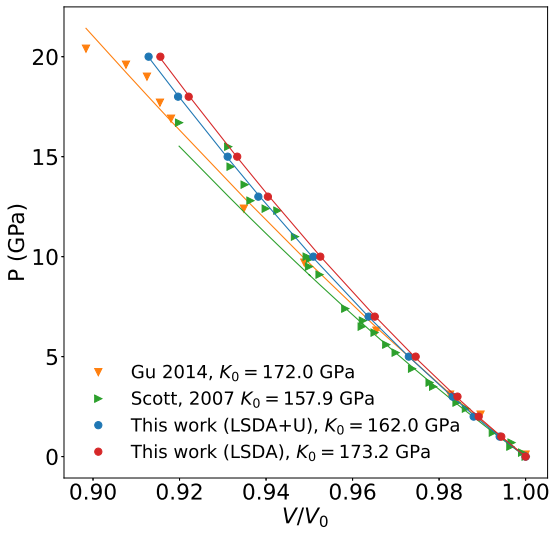

(a)

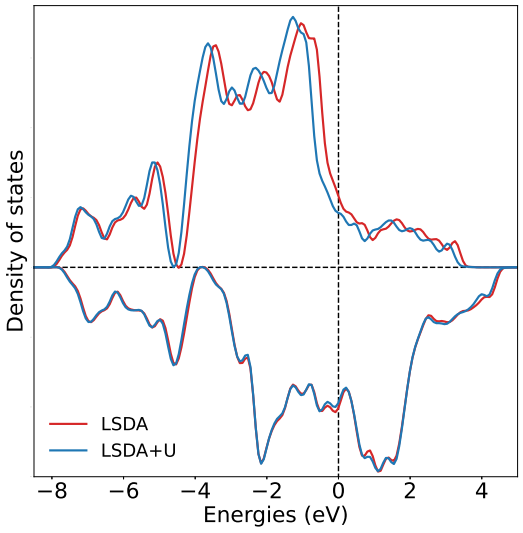

(b)

Figure 2: (a) Volume-pressure curve of Fe_3P. Points represent experimental[44,45] or calculated data, and solid lines the respective fit with a 2nd order Birch-Murnaghan equation of state. (b) Calculated electronic density of states (spin up and spin down) for bulk schreibersite with and without LSDA+U correction. The DOS was shifted to have zero energy at the Fermi energy.

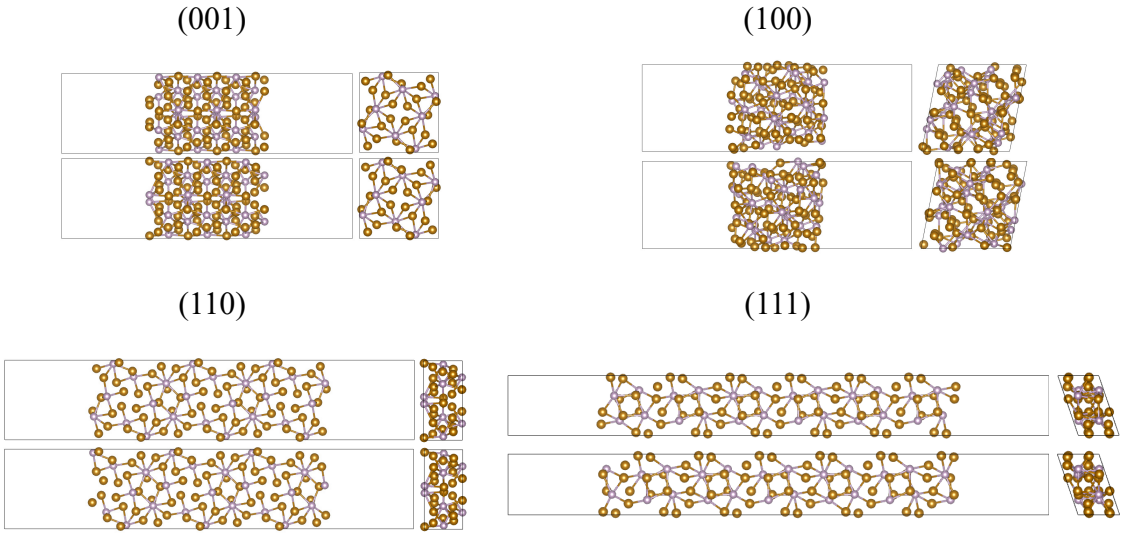

Figure 3: (*ac*) and (*ab*) view of the facets obtained from the bulk structure. Color code for atoms is the same as adopted in Fig. 1b

of 20 Å along the direction perpendicular to the slab surface (see Figs. S2 and S3 in the Supporting Information for more details). In order to improve computational efficiency, we have used the standard approach of fixing the positions of some non-surface atoms in order to replicate surface-bulk interactions.[38,46,51] In our case, we included a total of three active atomic layers between the top and the bottom surface of the slabs (i.e., roughly 1.5 atomic layers for each), while excluding the remaining atoms in the internal layers by freezing their degrees of freedom.

Table 2 shows our results for the surface energy for each facet and surface termination type, using LSDA+U. We find in general that the surface termination type with a larger phosphorus concentration yields lower surface energies. The difference between the two surface termination types is particularly dramatic for the (110) surface, which yields by far the lowest value for the type 2 surface (excess phosphorus) and the highest value for the type 1 surface (iron-rich), with a difference of $\sim$1 J/m^2. In contrast, the energetic ordering of the (100) surface is slightly lower for type 1 compared to type 2, with a difference of $\sim$0.1 J/m^2. The remaining (001) and (111) surface energies indicate that the type 2 termination is lower in energy overall by $\sim 0.20 - 0.25$ J/m^2. These results show similar trends to previous

Table 2: Converged surface formation energies E_{surface} from LSDA+U for the slabs represented in Fig. 3.

Surface orientation	termination	E_{surface} (J/m^2)
001	1	2.242
	2	2.005
100	1	1.949
	2	2.047
110	1	2.530
	2	1.540
111	1	2.066
	2	1.983

computational data obtained for (Fe_2,Ni)P,[46] where DFT calculations also indicated that (110) facet is the most stable.

In order to investigate the effect of the LSDA+U Hubbard correction on the surface facets, we have also computed the formation energies with standard DFT for the most stable (lowest energy) surface for each facet (Fig. 4). In general, we find that use of the LSDA+U correction lowers the surface energy by ∼10% overall, compared to a 3% reduction for the bulk energy (not shown here). However, for the most stable surface studied here, i.e., the (110) facet with type 2 termination, both LSDA+U and standard results agree within 2%. This provides additional justification for removing the correction for surface chemical studies on this surface facet, specifically.

We now investigate water adsorption and dissociation on the (110) facet with a type 2 termination. For this surface, three general adsorption sites can be defined and will be referred to as 'ontop', 'bridge' and 'hollow'. Although these terms are self-explanatory, it is worth mentioning that due to the binary nature of Fe_3P schreibersite, each type of site can involve different combinations of Fe or P atoms, resulting in two different sites types for each classification. We thus compute results for ontop sites on an iron or on a phosphorous atom, bridge sites among two iron atoms or one iron and one phosphorous, and two different hollow sites, with or without phosphorus, depending on the packing of the surface atoms

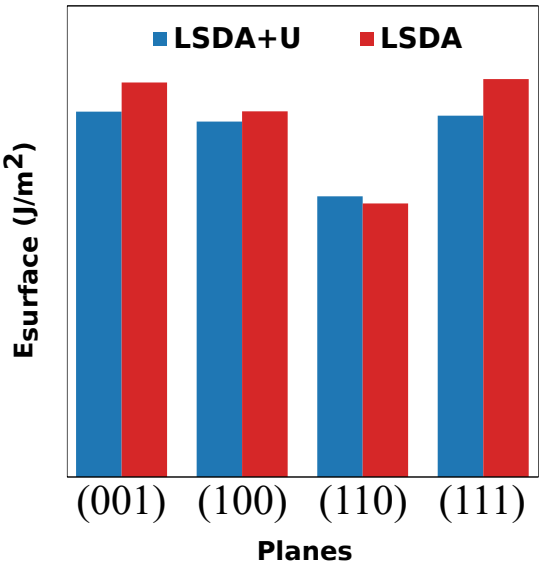

Figure 4: Comparison for the surface formation energies calculated with and without Hubbard correction, obtained for the most stable structures reported in Tab. 2.

(Fig. 5).

For each one of these sites, we defined three different orientations for the water molecule in its initial state, depending on the position of the H_2O molecular plane with respect to the plane of the schreibersite surface. In particular, we considered the 'planar' configuration in which the molecular plane is parallel to the slab surface (the molecule is essentially lying flat above the surface), and two orientations which we named as 'upward' and 'downward', in which the bisector of the HOH angle is perpendicular to the slab surface and the oxygen lies above the the hydrogen atoms or vice-versa, respectively (e.g., the water dipole moment points either up or down). We defined adsorption energy according to the following relation

$$E_{\text{ads}} = E_{\text{slab+H}_2\text{O}} - (E_{\text{slab}} + E_{\text{H}_2\text{O}}) \tag{2}$$

where $E_{\text{slab+H}_2\text{O}}$ is the energy of the Fe_3P slab with the adsorbed molecule in its final state, E_{slab} is the energy of the pristine slab, and $E_{\text{H}_2\text{O}}$ is the energy of an isolated water molecule obtained in a simulation cell as large as the one containing the schreibersite slab. We report

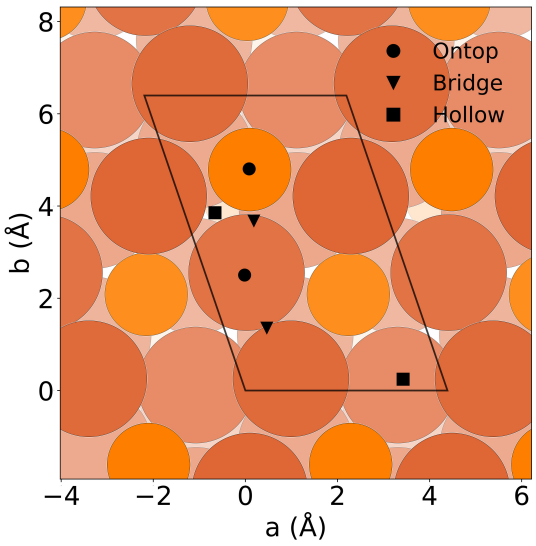

Figure 5: Different adsorption sites on (110) surface. In this image the big brown circles represent iron atoms, while the smaller orange circles stand for the phosphorous atoms.

the adsorption energies obtained for the different adsorption sites in Table 3.

The reported data show clearly that the water-schreibersite interaction is a physisorption phenomenon, where the adsorbate binds to the surface by weak van der Waals interactions. This is suggested by adsorption energies that are smaller than those of chemical bonding (e.g., < 1 eV) and by the relatively large distances from the slab surface. In general, the outcome of most of these calculations yielded a water molecular geometry that was parallel to the surface or at least reoriented towards that direction. Moreover, setting the molecular initial state in an upward or downward position generally did not make any substantial difference in terms of its final state since the adsorption energies for a given site tended to be close to isoenergetic. The small differences between similar energies are caused by different position of the molecule relative to the substrate in the (ab) plane, mostly due a molecular drift during the geometry relaxation procedure (see Supporting Information for a discussion about the initial and final molecular orientation on some adsorption sites). We found that instances with higher (more positive) energies (e.g., > -0.2 eV) yielded a final state with the molecular plane of the adsorbate close to perpendicular to the substrate surface, with one

Table 3: Adsorption energies, calculated from Eq. (2) for the different sites shown in Fig. 5, and for the three molecular orientations investigated here. We note that 'p' stands for planar, 'u' for upward, and 'd' for downward.

site		Initial orientation	E_{ads} (eV)
ontop	Fe	p	-0.227
		u	-0.269
		d	-0.268
	P	p	-0.173
		u	-0.162
		d	-0.164
Bridge	Fe-Fe	p	-0.429
		u	-0.444
		d	-0.445
	Fe-P	p	-0.211
		u	-0.168
		d	-0.184
Hollow	Fe-Fe-P	p	-0.331
		u	-0.338
		d	-0.334
	Fe-Fe-Fe	p	-0.195
		u	-0.484
		d	-0.484

hydrogen site pointing down towards the surface (molecular dipole parallel to the surface). This is in contrast to the upward and downward initial configurations, where both hydrogen sites were either above or below the oxygen site.

In addition, our results indicate that water adsorption tends to be more stable when the molecule lies closer to iron atoms or it is mostly surrounded by iron. We now discuss water adsorption on the Fe-Fe bridge and Fe-Fe-Fe hollow sites further, given that these are the lowest (strongest) adsorption interactions probed in our study. We observe that the final optimized state is characterized by a planar configuration, despite the initial downward orientation shown here (Figs. 6a and 6b). The low adsorption energies can be attributed in part to the under-coordinated environment of the iron atom closest to the adsorbate. If we consider a cut-off radius of $r = 4.$ Å (roughly two times the van der Waals radius of iron), the iron atom has a total of $n = 7$ neighbors. In contrast, the iron atom responsible for the higher energy ontop adsorption has $n = 10$ neighbors within the same radius.

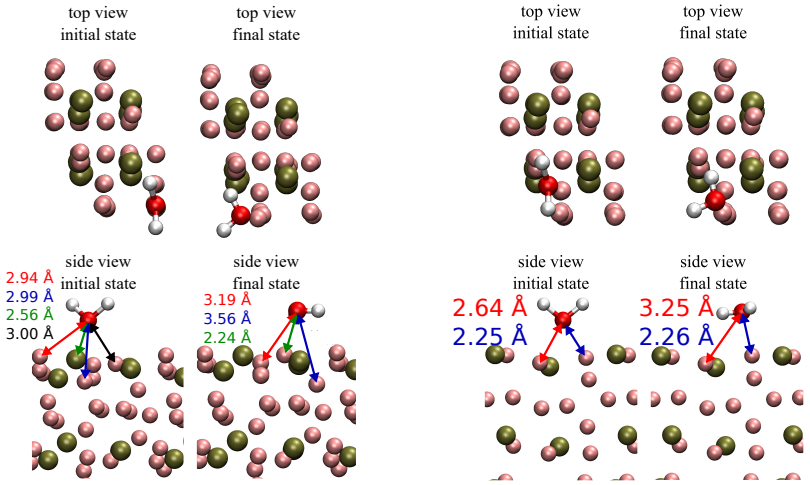

(a) Hollow Fe-Fe-Fe (b) Bridge Fe-Fe

Figure 6: Top and side view of the initial state and the fully relaxed geometry of water adsorbed on the schreibersite (110) surface. The distances reported on the side view are in Å. The side-views of each adsorption have been rotated an arbitrary amount for the sake of clarity.

We now investigate possible water dissociation reactions on the same (110) type 2 terminated surface. A widely adopted approach to determine the dissociation minimum energy

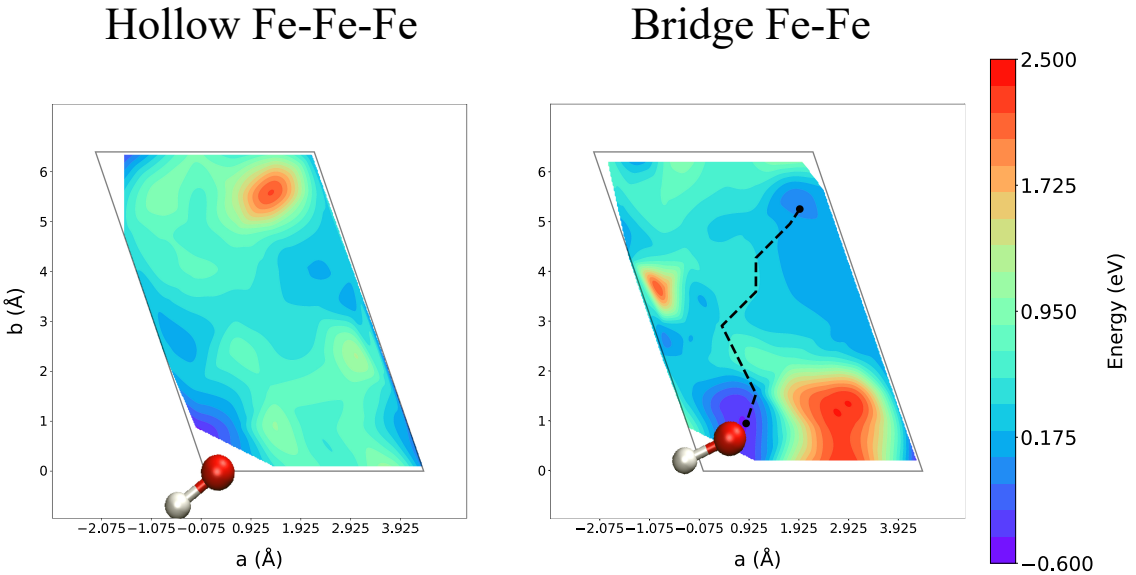

Figure 7: Energy grid calculations obtained for hollow Fe-Fe-Fe and bridge Fe-Fe adsorption with the OH^- ion held fixed in the adsorption site and the H^+ translated on our predefined grid. The dashed black line represents one possible minimum energy pathway for possible water dissociation

pathway is the nudged elastic band method (NEB).[52] Unfortunately, NEB and similar methods can be computationally intensive due to the involved number of calculations and the difficulty in choosing an appropriate initial guess for the minimum energy pathway. Instead, we adopt an energy grid approach,[38] which is computationally efficient and has been shown to provide reasonable initial estimates for the reaction barriers and pathways that can be probed with more expensive but accurate approaches at a later date.[53] Here, we initially hold fixed the position of the OH^- ion above a specific adsorption site. We then define a grid of points spanning one lattice displacement along each axis in increments of 0.75 Å where we move an H^+ ion to probe the potential energy surface of such a defined configuration. We then perform surface normal optimizations where only the positions of both OH^- and H^+ ions relative to the Fe_3P surface are allowed to vary (including relaxtion of the surface mobile iron and phosphorous atoms). In this way, we can determine estimates of the total potential energy for H_2O dissociation, including the manifold of possible dissociation and subsequent hydrogen diffusion pathways from the hollow Fe-Fe-Fe and the bridge Fe-Fe adsorption sites.

Our results are summarized in the two heat maps of Fig. 7. In the case of the Fe-Fe-Fe

hollow site (left panel), our results do not reveal any likely dissociation pathways, as the dissociated product is always ∼1 eV or greater in energy, compared to the relatively shallow adsorption energy of the OH^- ion . We do not observe any obvious saddle points on this energy surface. We also observe that the least favorable position for the H^+ ion is obviously the region surrounding the hydrogen atom of the hydroxide ion due to repulsive interactions (shifted to the upper right corner of the (ab) plane due to periodic boundary conditions). The rest of the potential energy surface in general exhibits rather flat behavior, with low energy regions close to the oxygen, suggesting additional (although less favorable) configurations for water adsorption.

On the other hand, the Fe-Fe bridge site (right panel) shows a markedly different energy landscape, characterized by overall lower adsorption energies for the dissociated system. Similar to the previous case, very high energy grid values are obtained when the dissociated hydrogen is placed close to the OH^- hydrogen. However, the central part of the plane suggest the presence of a saddle point which can be used to identify an approximate minimum energy path. In this pathway, the reaction $H_2O \rightarrow OH^- + H^+$ is characterized by an activation energy of roughly 0.4 eV (see Supporting Information, Fig. S7). Thermal activation is thus very unlikely under ambient conditions, since $kT = 0.0259$ eV at $T = 300$. Hence, these two bounding cases of reactivity appear unlikely to yield observable molecular dissociation.

We have investigated additional possible dissociation mechanisms from within the Fe-Fe bridge site by reversing our previous energy grid calculations. For this effort, we keep fixed the hydrogen ion in the bridge site, instead, and translate the OH^- ion along our radial grid. Again, the grid points were defined spanning the transverse axes in increment of 0.75 Å, although the hydrogen of the OH^- was initially randomly rotated with the O–H bond distance set to its equilibrium value ($d_{OH} = 0.98$ Å). In this way, this potential energy surface was explored while minimizing spurious results arising from an ordered grid of OH ions.

For this energy landscape, we observe two possible dissociation pathways (Fig. 8). One region of the surface displayed a distinct saddle point (black dashed line in the figure),

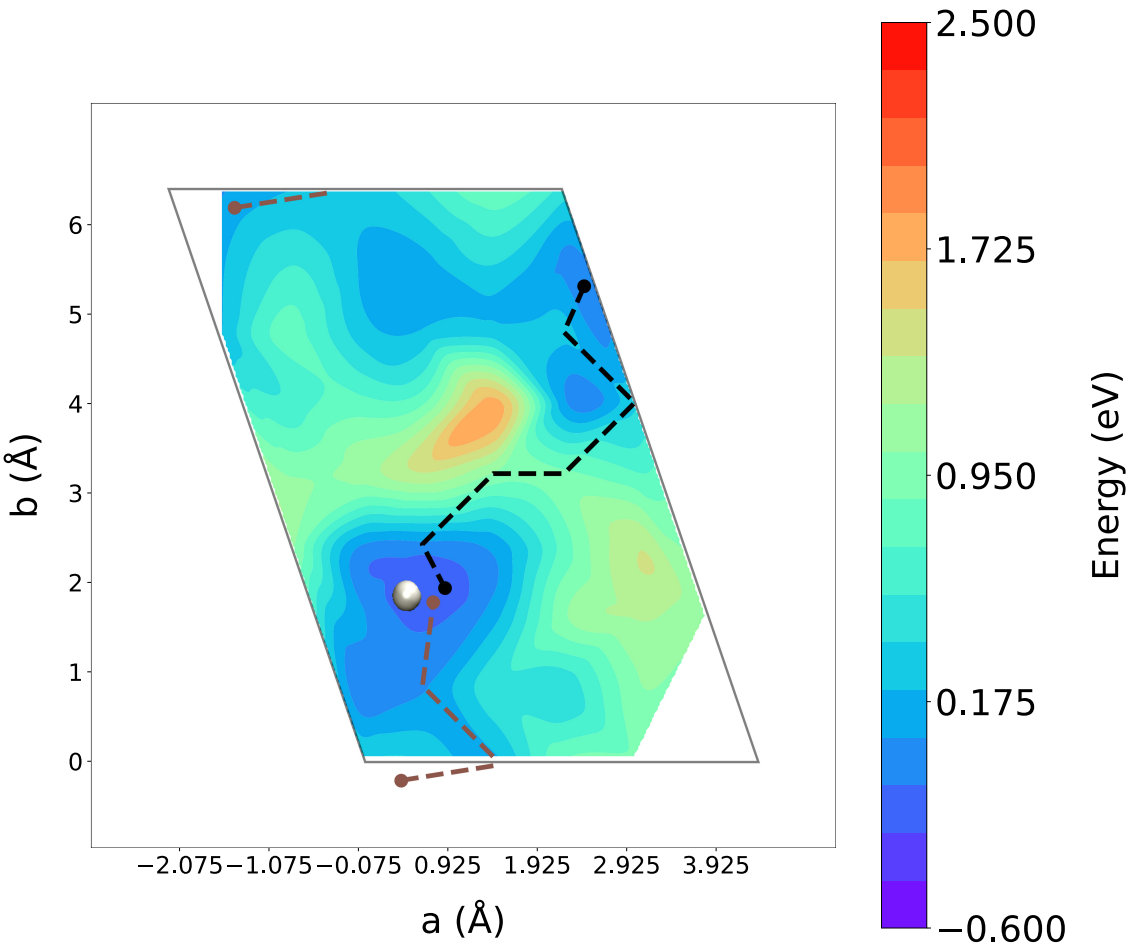

Figure 8: Energy grid calculations obtained for the bridge Fe-Fe adsorption site reported in Fig. 6b. Here, a randomly oriented OH^- ion was translated along predefined grid points in order to probe the energy landscape while keeping fixed the H^+ in its original adsorption site (shown as a white sphere). The two dashed lines represent the two possible reaction pathways discussed in the text. The broken dashed brown line at the top of the plot is a consequence of the periodic boundary conditions imposed in our simulation, and is extended to the bottom of the (ab) plane for the sake of clarity.

corresponding to a likely transition state for dissociation that could be examined further via NEB calculation. This reaction pathway yields a reaction energy of approximately zero, since both the adsorbed H_2O molecule and dissociated ions are roughly equal in energy. However, we estimate the reaction barrier to be ~ 1.0 eV, making it unlikely to be thermally activated under ambient conditions. We also observe a second possible reaction pathway (brown dashed line), in which adsorption of the dissociated ions (with H^+ residing in the Fe-Fe bridge site) is roughly iso-energetic to water adsorbed in the same site. For this reaction, we estimate the barrier to be $\sim$ 0.14 eV (see Supporting Information, Fig. S8), which is relatively low and thus significantly more likely to be thermally activated at moderate temperature.

We note that previous experimental studies performed on $(Fe_2, Ni)P$ schreibersite[22] suggest spontaneous corrosion in water, possibly in part along the low-energy pathway discussed here. However, our study has been conducted on a single, terraced, and defect free crystal facet in the dilute limit, only. In contrast, experiments have examined significantly higher water concentrations (with submerged samples) and likely probed poly-crystalline systems. Poly-crystalline materials in particular are likely exhibit a number of high energy and kinked facets known to promote chemical reactivity.[54] In addition, grain boundaries within solid system frequently contain amorphous regions,[55] which can also promote reactivity due to their distribution of non-stoichiometric states. Lastly, conditions on early Earth were likely highly volatile and spanned a large range of pressure and temperatures, in part due to impacts with meteorites and other astrophysical bodies. Regardless, our results represent an important first set of bounding calculations in elucidating possible scheibersite corrosion and phosphate ion production. Our future efforts will explore all of the possibilities discussed above, where will be be able to develop an ensemble of likely prebiotic organophosphate syntheses.

Conclusions

In this work we have conducted extensive first principles calculations aimed at characterizing the bulk structure of Fe_3P schreibersite and its surfaces. We determined the formation energies of low Miller index surfaces and investigated water adsorption on the schreibersite most stable facet, namely the (110) surface. We found that a single water molecule interacts weakly via physisorption, and that it tends to stay in a planar configuration with respect to the surface. Energy grid calculations on the (110) surface were carried out, showing that spontaneous dissociation does not occur from the hollow Fe-Fe-Fe sites. A possible thermally activated dissociation pathway was found from the Fe-Fe bridge site, although the net energy change in the reaction is very small. However this work only focused on a single, ideal (110) surface slab and in the dilute water limit. Regardless, the data reported here are amongst the first computational results to characterize Fe_3P schreibersite surface chemistry. All of our efforts yield necessary initial constraints for determining the role scheibersite might have played in prebiotic phosphorus chemistry.

Future work will include probable kinked and high energy surfaces in our calculations that are known to promote dissociation. Moreover, an accurate characterization of schreibersite phosphorylation on early Earth could require the investigation of shock compression conditions, where the simultaneous the effect of heating and pressurization likely yielded rapid and complex reactions. Our efforts will ultimately give us the opportunity to answer long standing questions in astrobiology regarding the catalysis of potentially life building compounds in aqueous environments.

Acknowledgement

This work was performed under the auspices of the U.S. Department of Energy by Lawrence Livermore National Laboratory under Contract DE-AC52-07NA27344. The authors gratefully thank the Exobiology Program Element NNH20ZDA001N-EXO for support (proposal

#20-EXO20-0149).

Supporting Information Available

References

(1) Miller, S. L. A production of amino acids under possible primitive Earth conditions. *Science* **1953**, *117*, 528.

(2) Miller, S. L. THE FORMATION OF ORGANIC COMPOUNDS ON THE PRIMITIVE EARTH. *Annals of the New York Academy of Sciences* **1957**, *69*, 260–275.

(3) Miller, S. L.; Urey, H. C. Organic compound synthesis on the primitive Earth. *Science* **1959**, *130*, 245.

(4) Harada, K.; Fox, S. Thermal synthesis of natural amino-acids from postulated primitive terrestrial atmosphere. *Nature* **1964**, *201*, 335–336.

(5) LaRowe, D.; Regnier, P. Thermodynamic potential for the abiotic synthesis of adenine, cytosine, guanine, thymine, uracil, ribose and deoxyribose in hydrothermal systems. *Origins of Life and Evolution of the Biosphere* **2008**, *38*, 383–397.

(6) Sagan, C.; Khare, B. N. Long-wavelength ultraviolet photoproduction of amino acids on the primitive Earth. *Science* **1971**, *173*, 417–420.

(7) Bernstein, M. P.; Dworkin, J. P.; Sandford, S. A.; Cooper, G. W.; Allamandola, L. J. Racemic amino acids from theultraviolet photolysis of interstellar ice analogues. *Nature* **2002**, *416*, 401.

(8) noz Caro, G. M. M.; Meierhenrich, U. J.; Schute, W. A.; Barbier, B.; Segovia, A. A.; Rosenbauer, H.; Thiemann, W. H.-P.; Brack, A.; Greenberg, J. M. Amino acids from ultraviolet irradiation of interstellar ice analogues. *Nature* **2002**, *416*, 403.

(9) Bar-Nun, A.; Bar-Nun, N.; Bauer, S. H.; Sagan, C. Shock synthesis of amino acids in simulated primitive environments. *Science* **1970**, *168*, 470.

(10) McKay, C. P.; Borucki, W. J. Organic synthesis in experimental impact shocks. *Science* **1997**, *276*, 390.

(11) Goldman, N.; Reed, E. J.; Fried, L. E.; Kuo, I.-F. W.; Maiti, A. Synthesis of glycine-containing complexes in impacts of comets on early Earth. *Nat. Chem.* **2010**, *2*, 949–954.

(12) Goldman, N.; Tamblyn, I. Prebiotic chemistry within a simple impacting icy mixture. *J. Phys. Chem. A* **2013**, *117*, 5124 – 5131.

(13) Martins, Z.; Price, M. C.; Goldman, N.; Sephton, M. A.; Burchell, M. J. Shock synthesis of organics from simple ice mixtures. *Nat. Geosci.* **2013**, *6*, 1045–1049.

(14) Kroonblawd, M. P.; Lindsey, R. K.; Goldman, N. Synthesis of Nitrogen-Containing Polycyclic Aromatic Hydrocarbons in Impacting Glycine Solutions. *Chemical Science* **2019**, *10*, 6091.

(15) Steele, B. A.; Goldman, N.; Kuo, I.-F. W.; Kroonblawd, M. P. Mechanochemical synthesis of glycine oligomers in a virtual rotational diamond anvil cell. *Chem. Sci.* **2020**, *11*, 7760–7771.

(16) Schwartz, A. W. Phosphorus in prebiotic chemistry. *Philos. Trans. R. Soc. Lond. B Biol. Sci.* **2006**, *361*, 1743–1749.

(17) Pasek, M. A.; Gull, M.; Herschy, B. Phosphorylation on the early earth. *Chemical Geology* **2017**, *475*, 149 – 170.

(18) Pasek, M. A. Schreibersite on the early Earth: Scenarios for prebiotic phosphorylation. *Geoscience Frontiers* **2017**, *8*, 329–335.

(19) Gull, M. Prebiotic Phosphorylation Reactions on the Early Earth. *Challenges* **2014**, *5*, 193–212.

(20) Gull, M.; Mojica, M. A.; Fernández, F. M.; Gaul, D. A.; Orlando, T. M.; Liotta, C. L.; Pasek, M. A. Nucleoside phosphorylation by the mineral schreibersite. *Scientific Reports* **2015**, *4*, 17198.

(21) Cruz, N. L. L.; Qasim, D.; Abbott-Lyon, H.; Pirim, C.; McKee, A. D.; Orlando, T.; Gull, M.; Lindsaya, D.; Pasek, M. A. The evolution of the surface of the mineral schreibersite in prebiotic chemistry. *Phys. Chem. Chem. Phys.* **2016**, *18*, 20160–20167.

(22) Pasek, M. A.; Dworkin, J. P.; Lauretta, D. S. A radical pathway for organic phosphorylation during schreibersite corrosion with implications for the origin of life. *Geochimica et Cosmochimica Acta* **2007**, *71*, 1721–1736.

(23) Pasek, M. A.; Lauretta, D. A. Aqueous Corrosion of Phosphide Minerals From Iron Meteorites: A Highly Reactive Source of Prebiotic Phosphorus on the Surface of the Early Earth. *Astrobiology* **2005**, *5*, 515–535.

(24) Bryant, D. E.; Kee, T. P. Direct evidence for the availability of reactive, water soluble phosphorus on the early Earth. H-Phosphinic acid from the Nantan meteorite. *Chem. Commun.* **2006**, *22*, 2344–2346.

(25) Manaa, M. R.; Reed, E. J.; Fried, L. E.; Goldman, N. Nitrogen-rich heterocycles as reactivity retardants in shocked insensitive explosives. *J. Am. Chem. Soc.* **2009**, *131*, 5493–5487.

(26) Kroonblawd, M. P.; Pietrucci, F.; Saitta, A. M.; Goldman, N. Generating Converged Accurate Free Energy Surfaces for Chemical Reactions with a Force-Matched Semiempirical Model. *J. Chem. Theory Comput.* **2018**, *14*, 2207–2218.

(27) Goldman, N.; Koziol, L.; Fried, L. E. Using force-matched potentials to improve the accuracy of density functional tight binding for reactive conditions. *J. Chem. Theory Comput.* **2015**, *11*, 4530–4535.

(28) Sours, T.; Patel, A.; Norskov, J.; Siahrostami, S.; Kulkarni, A. Circumventing Scaling Relations in Oxygen Electrochemistry Using Metal-Organic Frameworks. *The Journal of Physical Chemistry Letters* **2020**, *11*, 10029–10036.

(29) Kresse, G.; Hafner, J. Ab initio molecular dynamics for liquid metals. *Phys. Rev. B* **1993**, *47*, 558–561.

(30) Kresse, G.; Hafner, J. Ab initio molecular-dynamics simulation of the liquid-metal–amorphous-semiconductor transition in germanium. *Phys. Rev. B* **1994**, *49*, 14251–14269.

(31) Kresse, G.; Furthmüller, J. Efficient iterative schemes for ab initio total-energy calculations using a plane-wave basis set. *Phys. Rev. B* **1996**, *54*, 11169–11186.

(32) Kresse, G.; Joubert, D. From ultrasoft pseudopotentials to the projector augmented-wave method. *Phys. Rev. B* **1999**, *59*, 1758–1775.

(33) Blöchl, P. E. Projector augmented-wave method. *Phys. Rev. B* **1994**, *50*, 17953–17979.

(34) Perdew, J. P.; Burke, K.; Ernzerhof, M. Generalized Gradient Approximation Made Simple. *Phys. Rev. Lett.* **1996**, *77*, 3865–3868.

(35) Methfessel, M.; Paxton, A. T. High-precision sampling for Brillouin-zone integration in metals. *Phys. Rev. B* **1989**, *40*, 3616–3621.

(36) Monkhorst, H. J.; Pack, J. D. Special points for Brillouin-zone integrations. *Phys. Rev. B* **1976**, *13*, 5188–5192.

(37) Dudarev, S. L.; Botton, G. A.; Savrasov, S. Y.; Humphreys, C. J.; Sutton, A. P. Electron-energy-loss spectra and the structural stability of nickel oxide: An LSDA+U study. *Phys. Rev. B* **1998**, *57*, 1505–1509.

(38) Goldman, N.; Morales, M. A. A First-Principles Study of Hydrogen Diffusivity and Dissociation on δ-Pu (100) and (111) Surfaces. *The Journal of Physical Chemistry C* **2017**, *121*, 17950–17957.

(39) Ong, S. P.; Richards, W. D.; Jain, A.; Hautier, G.; Kocher, M.; Cholia, S.; Gunter, D.; Chevrier, V. L.; Persson, K. A.; Ceder, G. Python Materials Genomics (pymatgen): A robust, open-source python library for materials analysis. *Computational Materials Science* **2013**, *68*, 314–319.

(40) Tran, R.; Xu, Z.; Radhakrishnan, B.; Winston, D.; Sun, W.; Persson, K. A.; Ong, S. P. Surface energies of elemental crystals. *Scientific Data* **2016**, *3*, 160080.

(41) Sun, W.; Ceder, G. Efficient creation and convergence of surface slabs. *Surface Science* **2013**, *617*, 53–59.

(42) Humphrey, W.; Dalke, A.; Schulten, K. VMD: Visual molecular dynamics. *Journal of Molecular Graphics* **1996**, *14*, 33–38.

(43) Momma, K.; Izumi, F. *VESTA3* for three-dimensional visualization of crystal, volumetric and morphology data. *Journal of Applied Crystallography* **2011**, *44*, 1272–1276.

(44) Scott, H. P.; Huggins, S.; Frank, M. R.; Maglio, S. J.; Martin, C. D.; Meng, Y.; Santillán, J.; Williams, Q. Equation of state and high-pressure stability of Fe3P-schreibersite: Implications for phosphorus storage in planetary cores. *Geophysical Research Letters* **2007**, *34*.

(45) High-pressure behavior of Fe3P and the role of phosphorus in planetary cores. *Earth and Planetary Science Letters* **2014**, *390*, 296–303.

(46) Pantaleone, S.; Corno, M.; Rimola, A.; Balucani, N.; Ugliengo, P. Ab Initio Computational Study on Fe2NiP Schreibersite: Bulk and Surface Characterization. *ACS Earth and Space Chemistry* **2021**, *5*, 1741–1751.

(47) Birch, F. Finite Elastic Strain of Cubic Crystals. *Phys. Rev.* **1947**, *71*, 809–824.

(48) Murnaghan, F. D. The Compressibility of Media under Extreme Pressures. *Proceedings of the National Academy of Sciences* **1944**, *30*, 244–247.

(49) Himmetoglu, B.; Floris, A.; de Gironcoli, S.; Cococcioni, M. Hubbard-corrected DFT energy functionals: The LDA+U description of correlated systems. *International Journal of Quantum Chemistry* **2014**, *114*, 14–49.

(50) Jr, V. L. C.; Cococcioni, M. Extended DFT+$U+V$ method with on-site and inter-site electronic interactions. **2010**, *22*, 055602.

(51) Goldman, N.; Browning, N. D. Gold Cluster Diffusion Kinetics on Stoichiometric and Reduced Surfaces of Rutile TiO2(110). *The Journal of Physical Chemistry C* **2011**, *115*, 11611–11617.

(52) Henkelman, G.; Uberuaga, B. P.; Jónsson, H. A climbing image nudged elastic band method for finding saddle points and minimum energy paths. *The Journal of Chemical Physics* **2000**, *113*, 9901–9904.

(53) Goldman, N.; Aradi, B.; Lindsey, R. K.; Fried, L. E. Development of a Multicenter Density Functional Tight Binding Model for Plutonium Surface Hydriding. *J. Chem. Theory. Comput.* **2018**, *14*, 2652–2660.

(54) Luttge, A.; Fischer, C.; Zhang, L.; Arvidson, R. Kink sites: A key to surface reactivity and dissolution kinetics. *Geochimica et Cosmochimica Acta* **2007**, *71*, A603–A603.

(55) Zhang, H.; Srolovitz, D. J.; Douglas, J. F.; Warren, J. A. Grain boundaries exhibit the dynamics of glass-forming liquids. *Proc. Natl. Acad. Sci. USA* **2009**, *106*, 7735–7740.

Graphical TOC Entry